Computational Design of High-Entropy Rare Earth Disilicates as Next-Generation Thermal/Environmental Barrier Coatings

Shiqiang Hao[1,2], Richard P. Oleksak[1], Ömer N. Doğan[1], Michael C. Gao[1]

[1]National Energy Technology Laboratory, Albany, OR 97321, USA

[2]NETL Support Contractor, Albany, OR 97321, USA

ABSTRACT

Development of advanced thermal/environmental barrier coating (T/EBC) materials possessing balanced thermal-mechanical properties is crucial to protect SiC-based ceramic composites from chemical and thermal attack for better performance of components in the hot section of gas turbine engines. In this work we utilize density functional theory (DFT) together with combinatorial chemistry methodology to design high-performance high-entropy rare earth disilicates (β-$RE_2Si_2O_7$ (RE=Yb, Y, Er, Lu, La, Ce,)) for enhanced phase stability, desired coefficient of thermal expansion (CTE), low lattice thermal conductivity and good mechanical properties. The CTE are determined by phonon calculations at different volumes within the quasi-harmonic approximation. The lattice thermal conductivities are evaluated by the Debye-Callaway model considering three phonon processes. We show that the solid solution of $YYbSi_2O_7$ exhibit lowered lattice thermal conductivity than pure cases and a good range of CTE. We also present good EBC candidate materials of $Er_{1/4}Lu_{1/4}Y_{3/4}Yb_{3/4}Si_2O_7$ and $Er_{1/2}Lu_{1/2}Y_{1/2}Yb_{1/2}Si_2O_7$ with very low lattice thermal conductivity < 0.23 W/m/K at 1500 K and a good match of average CTE (5.1 - 5.2×10^{-6} K^{-1}) with SiC without compromising mechanical properties. These new EBC with outstanding multi-functional properties are believed to enable significant increases in the performance of protective components in gas turbines. This work also illustrates an efficient and reliable computational framework in accelerating the design of next-generation T/EBC.

Keywords*: Environmental barrier coating, rare earth elements, high entropy materials, first principles, thermophysical properties*

1. Introduction

Gas turbine engines have a huge impact on the transportation, energy, and defense sectors of the global economy. Due to the considerable economic presence in the rapidly growing sectors, there is a great interest for the development of better performing components in the hot section of gas turbine engines. In the practical engine applications, it is common to experience extremely high temperatures (e.g., up to 1800 K) [1] with corrosive species in the exhaust gas. Under these harsh conditions, thermal/environmental barrier coatings (TEBCs) are required to protect the current SiC-based ceramic matrix composite (CMC) [2] gas turbine components from significant degradation caused by reaction with water vapor and other corrosive species. Therefore, significant research efforts have focused on discovering novel T/EBC materials to enable higher temperature operation and improved efficiencies in gas turbine applications [3].

It is known that SiC-based ceramic matrix composites can fulfil the stringent requirements to provide an increased service temperature and superior strength at high temperatures in gas turbines. The corresponding EBC materials are expected to fulfil a set of protection requirements to be considered fit for service. Typically, there are several aspects that need to be considered for an effective EBC materials [4]. Due to the presence of heating and cooling cycles during service, thermal expansion and contraction will take place for each of the components of the EBC. If the magnitudes of their coefficient of thermal expansion (CTE) are too different from each other, the thermal stresses induced will lead to crack initiation and spallation along the interface. Therefore, the first important characteristic of the EBC material is a good CTE match with SiC-based ceramic matrix composite. Secondly, the desired EBC materials should have relatively high-phase stability to avoid crack initiation and porosity formation induced by undesirable phase transformation at high temperatures. Thirdly, a good chemical compatibility between the layers should be achieved to avoid reactions between the involved compositions that may produce unwanted byproducts when exposed to high temperatures for extended periods of time.

The objective of this work is not only to search for excellent multi-functional T/EBC materials with desirable properties using density functional theory (DFT) calculations, but also to provide a computational strategy for designing high temperature materials with multi-functional properties requirements derived from an insightful understanding of the physical origins of their mechanical and thermal properties. In this study, we focus on computational design of high-

performance high entropy rare earth pyrosilicates ($RE_2Si_2O_7$, where RE =Y, La, Ce, Er, Yb, and Lu). Alloy design is based on encouraging experimental results reported in the literature such as b-$Y_2Si_2O_7$ and b-$Y_2Si_2O_7$ that demonstrate good corrosion resistance against CMAS attack – key property for EBC and high entropy alloy concept that can lead to ultralow thermal conductivity – key property for TBC. Rare earth pyrosilicates such as β-$Yb_2Si_2O_7$ are identified as promising candidate materials for EBC applications due to their thermal stability at high temperatures, high resistance to oxidation and corrosion, and possible good match of CTE with the Si-based CMCs [5]. We utilize a computational combinatorial chemistry methodology to tailor the functional properties of $RE_2Si_2O_7$. The mixing of yttrium and ytterbium with other rare earth elements in the cation site increases the configurational entropy and hence lowers the free energy of $RE_2Si_2O_7$, suppressing the undesirable decomposition reaction from disilicate to mono-silicate (e.g. $Yb_2Si_2O_7 \rightarrow Yb_2SiO_5 + SiO_2$) to preventing crack formation by the decomposition-induced volume changes. It is expected that doping Er, Lu and Ho will stabilize β $Yb_2Si_2O_7$ due to their similar RE^{3+} ionic radii [3] and the contribution to the β phase stability from increased entropy of mixing in the Yb sublattice. Furthermore, β-$Er_2Si_2O_7$ and β-$Lu_2Si_2O_7$ have CTE values similar to SiC [3]. Experiments by Chen at al. [6] demonstrated that high entropy rare earth pyrosilicates such as $(Yb_{0.2}Y_{0.2}Lu_{0.2}Ho_{0.2}Er_{0.2})_2Si_2O_7$ and $(Yb_{0.25}Lu_{0.25}Ho_{0.25}Er_{0.25})_2Si_2O_7$, indeed increase the beta phase stability towards lower temperature and corrosion resistance against calcium magnesium aluminum silicate (CMAS) molten salt corrosion.

Therefore, in this work we focus on the (Er, Lu, Y, Yb)$_2Si_2O_7$ system and also study the effect of doping La and Ce that are significantly cheaper than Lu or Yb. Furthermore, the lattice thermal conductivities of the mixed $RE_2Si_2O_7$ are expected to be lower than the average value estimated using the rule of mixtures (ROM) due to mass fluctuation and lattice distortion-induced phonon scatterings. Low lattice thermal conductivity of the coating is crucial to a protective coating because it significantly reduces the thermal stress to the SiC-based composites and avoids unnecessary high temperature chemical reactions. More importantly, the combinatorial chemistry method also provides a practical way to tune CTE to a desired range by adjusting chemical species and chemical compositions. Finally, we present promising EBC candidate materials with very low lattice thermal conductivity and a good match of CTE with SiC awaiting experimental confirmation.

2. Calculations

2.1 Density Functional Theory (DFT) Calculations

The total energies and relaxed structural configurations of $RE_2Si_2O_7$ were calculated by DFT as implemented in the Vienna *ab initio* simulation package [7]. The electron-ion interactions were described through projector augmented wave [8] and the exchange-correlation functional was constructed by the generalized gradient approximation (GGA) proposed by Perdew-Burke-Ernzerhof [9]. The total energies were numerically converged to approximately 1 meV/atom with spin-orbit coupling using a basis set energy cutoff of 550 eV and dense *k*-meshes corresponding to 4000 per reciprocal atom *k*-points in the Brillouin zone. The conjugate gradient method was chosen to relax the structure of atomic positions, cell volumes, and cell shapes. To accurately deal with rare-earth f-state electrons [10], researchers often employ techniques like DFT+U or higher order functionals such as HSE06 to avoid self-interaction errors. However, utilizing HSE06 can be too costly for our specific project. Our systems involve large cell sizes, ranging from at least 22 atoms to up to 88 atoms for solid solutions, making phonon calculations infeasible. As for the DFT+U method, its reliance on the empirical and case-specific U parameter made it less preferable for our project. To address the f-state electrons in rare-earth elements, we opted for using PAW potentials that treat the 4f electrons as core electrons. By doing so, we ensured that the formation energy and corresponding thermodynamic behavior remained unaffected by the f-state electrons. Moreover, we used ferromagnetic spins for rare earth elements with an initial magnetic moment of 5 μB.

2.2 Cluster Expansion

The cluster expansion (CE) approach was used to construct an effective Hamiltonian for energy evaluation on the monoclinic structure. We used the ATAT toolkit to obtain the optimal effective cluster interactions from fully relaxed total energies of ordered input structures [11]. In a typical simple binary cluster expansion, the energy is expressed as $E(\sigma) = \sum_\alpha m_\alpha J_\alpha \langle \prod_i \sigma_i \rangle$ with a spin variable σ_i with a value of ±1 that denotes the type of atom sitting on each site *i*, where m_α and J_α are multiplicities and effective interactions of cluster type α. By fitting 35 ordered input structures, the final cluster expansion contains 11 interaction coefficients, including nine two-body interactions, resulting in a leave-one out cross-validation score as 1.7 meV/cation, which is only approximately 5% of the most favorable formation energy of -35 meV. The formation energy ΔH of a $A_{1-x}B_x$ with respect to the energies of constituents A and B

is defined as $\Delta H(\sigma) = E_{tot}(\sigma) - (1-x)E_{tot}^{A} - xE_{tot}^{B}$, where $E_{tot}(\sigma), E_{tot}^{A}$, and E_{tot}^{B} are total energies of phases $A_{1-x}B_x$, A, and B, respectively. For example, the formation energies of $Y_{1-x}Yb_xSi_2O_7$ ($A_{1-x}B_x$) are calculated with respect to the references of β–$Y_2Si_2O_7$ (A) and β $Yb_2Si_2O_7$ (B).

Based on the converged effective cluster interactions, the order-disorder transition temperatures were calculated by Canonical Monte Carlo simulations [12]. In the canonical ensemble, the energy and concentration of an alloy (with a fixed total number of atoms) are allowed to fluctuate while temperature and chemical potentials are externally imposed. By scanning over temperature and chemical potentials, the two-phase regions in the phase diagram can be determined from discontinuities of composition as a function of chemical potential. We used a 40 × 40 × 40 unit cell as the simulation cell, and the simulated temperatures ranged from 25 to 800 K with a 25 K interval. We used 40,000 MC steps to equilibrate and 100,000 MC steps for averaging, and we monitored the composition change with chemical potential at a given temperature. The thermodynamic state was thus determined as a function of the temperature and the chemical potential differences of the constituents.

2.3 Elastic Constants and Mechanical Properties

We applied the strain-energy methods to evaluate the elastic constants. The total energy of a crystal under any small strain, δ, can be expressed in a Taylor series in powers of the strain tensor with respect to that of the unstrained crystal,

$$E(V,\delta) = E(V_0,0) + V_0\left(\sum_i \tau_i\xi_i\delta_i + \frac{1}{2}\sum_{i,j} c_{ij}\,\delta_i\xi_i\delta_j\xi_j\right) + O(\delta^3) \quad (1)$$

A series of DFT calculated total energies of $E(V,\delta)$ for strained cell and $E(V_0,0)$ for equilibrium cell are necessary. By neglecting the higher order of strained energy contribution $O(\delta^3)$, the elastic constant can be calculated by a second derivative of the strain-induced energy change with respect to different direction of strains when the stress τ is zero:

$$c_{ij} = \frac{1}{V_0}\left(\frac{\partial^2 E}{\partial\delta_i\partial\delta_j}\right)_{\tau=0} \quad (2)$$

For the monoclinic systems, the 13 independent elastic constants can be obtained by applying 13 distortions [13]. The 13 independent parameters include six diagonal components C_{ii}

(i=1, 2, 3, 4, 5, 6) and seven off-diagonal components of C_{12}, C_{13}, C_{15}, C_{23}, C_{25}, C_{35}, and C_{46} as listed in the Equ. (3):

$$\begin{pmatrix}\sigma_{11}\\ \sigma_{22}\\ \sigma_{33}\\ \sigma_{23}\\ \sigma_{13}\\ \sigma_{12}\end{pmatrix} = \begin{pmatrix}C_{11} & C_{12} & C_{13} & 0 & C_{15} & 0\\ C_{12} & C_{22} & C_{23} & 0 & C_{25} & 0\\ C_{13} & C_{23} & C_{33} & 0 & C_{35} & 0\\ 0 & 0 & 0 & C_{44} & 0 & C_{46}\\ C_{15} & C_{25} & C_{35} & 0 & C_{55} & 0\\ 0 & 0 & 0 & C_{46} & 0 & C_{66}\end{pmatrix}\begin{pmatrix}\varepsilon_{11}\\ \varepsilon_{22}\\ \varepsilon_{33}\\ 2\varepsilon_{23}\\ 2\varepsilon_{13}\\ 2\varepsilon_{12}\end{pmatrix} \quad (3)$$

For each elastic constant, six different magnitudes of strains ±0.7%, ±1.4%, ±2.1% were applied to the corresponding DFT relaxed equilibrium structures of β $RE_2Si_2O_7$, so that the elastic constants could be extracted. A fourth-degree polynomial was fitted to the corresponding DFT calculated energies thus defining the harmonic coefficient, relevant for the elastic constants. Note that we adopted the relatively small magnitude of strains upon the lattice to ensure the energy landscape was not dominated by higher-order phonon-phonon interactions to avoid the phonon mode instabilities that the quasi-harmonic approximation does not account for.

It is worth mentioning that for a mechanically stable structure the elastic constants must meet the mechanical stability criteria [27]. The mechanical stability criteria for a monoclinic system are listed in Equ. (4). With the elastic constants, the bulk and shear moduli can be evaluated by the Equ. (5).

$C_{ii} > 0$ (i=1,2,3,4,5,6);

$C_{11} + C_{22} + C_{33} + 2(C_{12} + C_{13} + C_{23}) > 0$;

$C_{33}C_{55} - C_{35}^2 > 0$;

$C_{44}C_{66} - C_{46}^2 > 0$;

$C_{33} + C_{33} - 2C_{23} > 0$;

$C_{22}(C_{33}C_{55} - C_{35}^2) + 2C_{23}C_{25}C_{35} - C_{23}^2C_{55} - C_{25}^2C_{33} > 0$;

$2[C_{15}C_{25}(C_{33}C_{12} - C_{13}C_{23}) + C_{15}C_{35}(C_{22}C_{13} - C_{12}C_{23}) + C_{25}C_{35}(C_{11}C_{23} - C_{12}C_{13})]$-
$[C_{15}C_{15}(C_{22}C_{33} - C_{23}^2) + C_{25}C_{25}(C_{11}C_{33} - C_{13}^2) + C_{35}C_{35}(C_{11}C_{22} - C_{12}^2)]$+ $gC_{55} > 0$;

$g = C_{11}C_{22}C_{33} - C_{11}C_{23}^2 - C_{22}C_{13}^2 - C_{33}C_{12}^2 + C_{12}C_{13}C_{23}$ (4)

To calculate average elastic properties for polycrystalline solids, such as bulk modulus, Young's modulus, shear modulus, and Poisson's ratio (ν), we adopt the Voigt-Reuss-Hill methods (see Equ. (5)). It is known that Voigt's scheme gives the upper bound with the elastic constant matrix input, while Reuss' method provides the lower bound by evaluating the elastic compliance matrix (inverse to the elastic-constant matrix), and Hill made an average on the Voigt and Reuss results.

$$9B_V = (C_{11} + C_{22} + C_{33}) + 2(C_{12} + C_{23} + C_{31});$$

$$15G_V = (C_{11} + C_{22} + C_{33}) - (C_{12} + C_{23} + C_{31}) + 3(C_{44} + C_{55} + C_{66});$$

$$1/B_R = (s_{11} + s_{22} + s_{33}) + 2(s_{12} + s_{23} + s_{31});$$

$$15/G_R = (s_{11} + s_{22} + s_{33}) - (s_{12} + s_{23} + s_{31}) + 3(s_{44} + s_{55} + s_{66});$$

$$B_H = 0.5(B_V + B_R);\ G_H = 0.5(G_V + G_R) \quad (5)$$

where $B_V(G_V)$, $B_R(G_R)$, and B_H (G_H) are the bulk modulus (shear modulus) according to Voigt, Reuss, and Hill methods, respectively.

On the basis of elastic constants C_{ij} and elastic compliance constants S_{ij}, the elastic anisotropy can be evaluated through directional dependence of Young's and shear moduli. The directional Young's and shear moduli are evaluated by

$$\frac{1}{E} = l_1^4 s_{11} + 2l_1^2 l_2^2 s_{12} + 2l_1^2 l_3^2 s_{13} + 2l_1^3 l_3 s_{15} + l_2^4 s_{22} + 2l_2^2 l_3^2 s_{23} + 2l_1 l_2^2 l_3 s_{25} + l_3^4 s_{33} + 2l_1 l_3^3 s_{35} + l_2^2 l_3^2 s_{44} + 2l_1 l_2^2 l_3 s_{46} + l_1^2 l_3^2 s_{55} + l_1^2 l_2^2 s_{66}$$

$$G_{(100)} = 1/(s_{44} + (s_{22} + s_{33} - 2s_{23} - s_{44})sin^2 2\theta)$$

$$G_{(010)} = 1/(s_{55} + (s_{11} + s_{33} - 2s_{13} - s_{55})sin^2 2\theta + (s_{15} + s_{35})sin 4\theta)$$

$$G_{(001)} = 1/(A + (B - A)sin^2 2\theta)$$

$$A = s_{44}sin^2\alpha + s_{66}cos^2\alpha - 2s_{46}cos\alpha sin\alpha$$

$$B = s_{11}cos^4\alpha + s_{22} + s_{33}sin^4\alpha - 2s_{12}cos^2\alpha + 2s_{13}cos^2\alpha sin^2\alpha - 2s_{23}sin^2\alpha - 2s_{15}cos^3\alpha sin\alpha + 2s_{25}cos\alpha sin\alpha - 2s_{35}cos\alpha sin^3\alpha + s_{55}cos^2\alpha sin^2\alpha \quad (6)$$

where S_{ij} is the elastic compliance constant, α is azimuthal angle, l_1, l_2, and l_3 are the directional cosines of angles with the three principal directions, respectively.

2.4 Phonon Dynamics

To investigate the temperature effect on the elastic constants, we considered the system Helmholtz free energy as a function of temperature by incorporating the vibrational enthalpy and entropy. It is necessary to evaluate the vibrational frequencies in the entire Brillouin zone to get a meaningful phonon energy contribution to the Helmholtz free energy. To represent the phonon vibrational frequencies, we depict phonon dispersion along the high symmetrical lines in the Brillouin zone. To calculate the phonon modes, we utilized the so-called finite atomic displacement methods [14], in which the force constant matrix is constructed by evaluating the total energies of a series of configurations with shifted distinct atoms in the cell away from their equilibrium positions. The dynamical matrix at any $\vec{q}$ point can be given by considering the masses of different species based on force constant matrix,

$$D_{ij}^{\alpha\beta}(\vec{q}) = \frac{1}{\sqrt{m_i m_j}} \sum_{l'} \Phi_{l_i l'_j}^{\alpha\beta} e^{i\vec{q}R_{l'}} \tag{7}$$

where m is the atomic mass, Φ is the harmonic interatomic force constant matrix, $R_{l'}$ is the translation vector of the unit cell l', ij specifies the i-th(j-th) atom in the primitive cell, and α, β are the Cartesian components. The numerical diagonalization of the dynamical matrix yields the eigenvalues and eigenvectors, which correspond to the phonon frequencies and the dispersion vectors, respectively.

The sum over phonon modes can also be formulated as an integral over the phonon density of states $g(\omega)$ on a sufficiently dense mesh of crystal momenta $\vec{q}$ in reciprocal space to evaluate $F(T, V)$ at all temperatures [15],

$$F(T,V) = \phi_0 + \int g(\omega) \left\{ \frac{\hbar\omega}{2} + k_B T \, ln\left(1 - e^{\frac{-\hbar\omega}{k_B T}}\right) \right\} d\omega \Big|_V \tag{8}$$

where the first term, ϕ_0, is the ground-state electronic energy of the system at equilibrium volume with zero atomic displacements, $g(\omega)$ is the phonon density of states, $\hbar\omega$ is the phonon energy, and T is the temperature. Note that the electronic contribution to the free energy is not

considered due to the metal oxide insulators. The Helmholtz free energy provides all the information that is needed to obtain the lattice parameters as a function of temperature. The elastic constants can then be calculated by a similar procedure mentioned previously, a second derivative of the strain induced Helmholtz free energy change with respect to different direction of strains when the stress τ is zero.

2.5 Coefficient of Thermal Expansion and Quasi-Harmonic Approximation

In the same manner as mechanical strain, the thermal energy can induce strains on the crystal lattice. In a non-cubic material, each unique crystallographic axis will generally have a different CTE α_{ij} value, because crystals typically expand or contract at different rates with temperature along different directions. The coefficient of volumetric thermal expansion α_V describes volumetric strain as a function of temperature through $\Delta V = \alpha_V \Delta T$, which is equivalent to the trace of the thermal expansion tensor with a unit of K^{-1}. In this work, we do not explicitly express the CTE tensor, rather give the coefficient of volumetric thermal expansion α_V as a function of temperature.

The origin of thermal expansion in solid materials is the anharmonicity of interatomic potential of the constituent atoms in the crystal lattice. The most important source of anharmonicity relevant to thermal expansion is the coupling between phonons and strain, which is characterized by the changes in the unit cell dimensions with temperature. In the quasi-harmonic approximation, we assume that each phonon acts as an independent harmonic oscillator, thus the energy of a single phonon mode does not depend on the occupation of any other phonon modes. In other words, the phonon frequencies are allowed to be volume dependent, which implies that the vibrational properties are calculated at least not only at the DFT relaxed equilibrium volume, but also isotropically expanded or contracted volumes.

2.6 Debye-Callaway Model for Lattice Thermal Conductivity

Several approaches have been used for lattice thermal conductivity calculations including second-order, third-order force constants [16], molecular dynamics, and compressive sensing [17] methods. Generally, the molecular dynamics and third-order force constant methods are time consuming, and therefore, we apply the Debye-Callaway model by incorporating the lattice vibrational properties as mentioned in the phonon dynamics section [18]. Within the Debye-Callaway formalism, we consider the most important three-phonon processes, namely, the

normal phonon scattering and Umklapp scattering [19]. To get the Grüneisen parameters as a necessary input for the Debye-Callaway model, we performed phonon dispersion calculations within the quasi-harmonic approximation. This method has recently been shown to produce accurate values of lattice thermal conductivity, compared to experiments, for a range of thermoelectric compounds [20]. The total lattice thermal conductivity can be written as a sum over one longitudinal κ_{LA} and two transverse κ_{TA} and $\kappa_{TA'}$ acoustic phonon branches: $\kappa_{Latt} = \kappa_{LA} + \kappa_{TA} + \kappa_{TA'}$. The partial conductivities κ_i (i corresponds to *TA*, *TA'*, and *LA* modes) are given by

$$\kappa_i = \frac{1}{3} C_i T^3 \left\{ \int_0^{\Theta_i/T} \frac{\tau_c^i(x) x^4 e^x}{(e^x-1)^2} dx + \frac{\left[\int_0^{\Theta_i/T} \frac{\tau_c^i(x) x^4 e^x}{\tau_N^i (e^x-1)^2} dx \right]^2}{\int_0^{\Theta_i/T} \frac{\tau_c^i(x) x^4 e^x}{\tau_N^i \tau_U^i (e^x-1)^2} dx} \right\} \quad (9)$$

In this expression, Θ_i is the longitudinal or transverse Debye temperature, $1/\tau_N^i$ is the scattering rate for normal phonon processes, $1/\tau_R^i$ is the sum of all resistive scattering processes, $1/\tau_c^i = 1/\tau_N^i + 1/\tau_R^i$, $x = \hbar\omega/k_B T$, and $C_i = k_B^4/2\pi^2\hbar^3 v_i$. Here, $\hbar$ is the Planck constant, k_B is the Boltzmann constant, ω is the phonon frequency, and v_i is the longitudinal or transverse acoustic phonon velocity.

The resistive scattering rate is the sum of scattering rates due to Umklapp phonon-phonon scattering ($1/\tau_U^i$), mass-difference impurity scattering ($1/\tau_m^i$), boundary scattering ($1/\tau_B^i$), and electron-phonon scattering ($1/\tau_{e-ph}^i$). In the pure single crystal compounds, we only consider the intrinsic thermal conductivity, and ignore the effect of impurity scattering. Due to relatively large band gaps, we thus neglect electron-phonon scattering contributions especially for temperatures above approximately 100 K. The resistive scattering rate is mainly determined by the Umklapp phonon-phonon processes ($1/\tau_R^i \cong 1/\tau_U^i$). The normal phonon scattering and Umklapp can be written as,

$$\frac{1}{\tau_N^{LA}(x)} = \frac{k_B^5 \gamma_{LA}^2 V}{M\hbar^4 v_{LA}^5} x^2 T^5 \quad (10)$$

$$\frac{1}{\tau_N^{TA/TA'}(x)} = \frac{k_B^5 \gamma_{TA/TA'}^2 V}{M\hbar^4 v_{TA/TA'}^5} x T^5 \quad (11)$$

$$\frac{1}{\tau_U^i(x)} = \frac{k_B^2 \gamma_i^2}{M\hbar v_i^2 \Theta_i} x^2 T^3 e^{-\theta_i/3T} \quad (11)$$

where γ, V, and M are the Grüneisen parameter, the volume per atom, and the average mass of an atom in the crystal, respectively. The Grüneisen parameter can be defined as, $\gamma_i = -\frac{V\partial\omega_i}{\omega_i \partial V}$, characterizing the relationship between phonon frequency and volume change.

3. Results

3.1 Atomic Structure

The β phase of $Y_2Si_2O_7$ has a monoclinic structure with C2/m space group and its atomic structure is shown in Figure 1, where the Si atoms are tetrahedrally coordinated with four oxygen-forming corner-sharing tetrahedra and the Y atoms form distorted octahedra with six surrounding oxygen atoms. The calculated lattice parameters are: a=6.88 Å, b=8.98 Å, c=4.72 Å, $\alpha = \gamma = 90°$, and $\beta = 101.61°$, as listed in the well-known material databases such as Open Quantum Materials Database OQMD [21]. Both β $Yb_2Si_2O_7$ and β $Y_2Si_2O_7$ are reported to be thermodynamically stable, thus, it is expected to get a stable mixing phase of the two phases, as conformed experimentally [22]. The lattice constants of the β phase of $Yb_2Si_2O_7$ are: a=6.82 Å, b=9.01 Å, c=4.76 Å, $\alpha = \gamma = 90°$, and $\beta = 101.48°$.

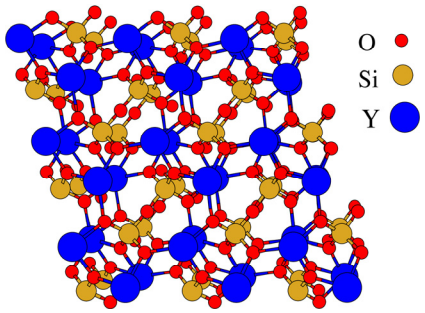

Figure 1 *The atomic structure of β phase of monoclinic $Y_2Si_2O_7$ with the space group of C2/m. The atomic structure of $Yb_2Si_2O_7$ is the same as $Y_2Si_2O_7$. The Si atoms are tetrahedrally coordinated with four oxygen-forming corner-sharing tetrahedra. The Y atoms form distorted octahedra with six surrounding oxygen atoms.*

For the atomic structure of $YYbSi_2O_7$, we first examined if the ordered compound is thermodynamically stable relative to the pure compounds $Y_2Si_2O_7$ and $Yb_2Si_2O_7$ at zero temperature. Using the DFT and cluster expansion computational methodology, we evaluated the

formation energy of all 35 ordered structures of β $Y_{2-x}Yb_xSi_2O_7$ ($0 < x < 2$) with less than 22 atoms per unit cell shown in Figure 2. By constructing the convex hull (the lowest-energy set of tie-lines such that no structure lies below the hull), we identified the ground state structures at 0 K as a function of composition. Figure 2(a) shows that the formation energies of the $Y_{2-x}Yb_xSi_2O_7$ structures are often positive, but some configurations are negative, indicating stability of the compounds relative to pure $Y_2Si_2O_7$ and $Yb_2Si_2O_7$ at zero temperature. The $Y_2Si_2O_7$ and $Yb_2Si_2O_7$ are in the same prototype monoclinic structure, and the relatively small lattice mismatch (<0.8%) induces a relatively small strain energy penalty, which directly explains negative formation energies [23-25]. It is evident from Figure 2(a) that there are three stable ground state structures, namely, $Y_{1/2}Yb_{3/2}Si_2O_7$, $YYbSi_2O_7$, and $Y_{3/2}Yb_{1/2}Si_2O_7$.

To identify the order-disorder transition temperature of $YYbSi_2O_7$ and $Y_{3/2}Yb_{1/2}Si_2O_7$, we also performed Canonical Monte Carlo simulations at these compositions to monitor the enthalpy change as a function of temperature. We found there is an abrupt energy increase at 360 K as shown in Figure 2(c), suggesting a first-order transition to a disordered phase with a higher energy for $YYbSi_2O_7$ system. Similarly, an order-disorder transition for $Y_{3/2}Yb_{1/2}Si_2O_7$ and $Y_{1/2}Yb_{3/2}Si_2O_7$ occurs at ~190 K. The calculation results clearly indicated that we predicted a stable ordered compound $YYbSi_2O_7$ at room temperature. The ordered atomic structure of $YYbSi_2O_7$ is illustrated in the Appendix awaiting future experimental confirmation.

Since we are interested in the thermal and mechanical properties at high temperatures, a solid solution of Y and Yb in the cation site of $Y_2Si_2O_7$-prototype is adopted for $YYbSi_2O_7$ to further predict its thermal and mechanical properties. The other rare earth species Er and Lu as well as La and Ce are considered to tune the thermal and mechanical properties by keeping the majority cation species Y and Yb, namely $Er_{1/4}Lu_{1/4}Y_{3/4}Yb_{3/4}Si_2O_7$, $Er_{1/2}Lu_{1/2}Y_{1/2}Yb_{1/2}Si_2O_7$, and $La_{1/4}Ce_{1/4}Er_{1/4}Lu_{1/4}Y_{1/2}Yb_{1/2}Si_2O_7$.

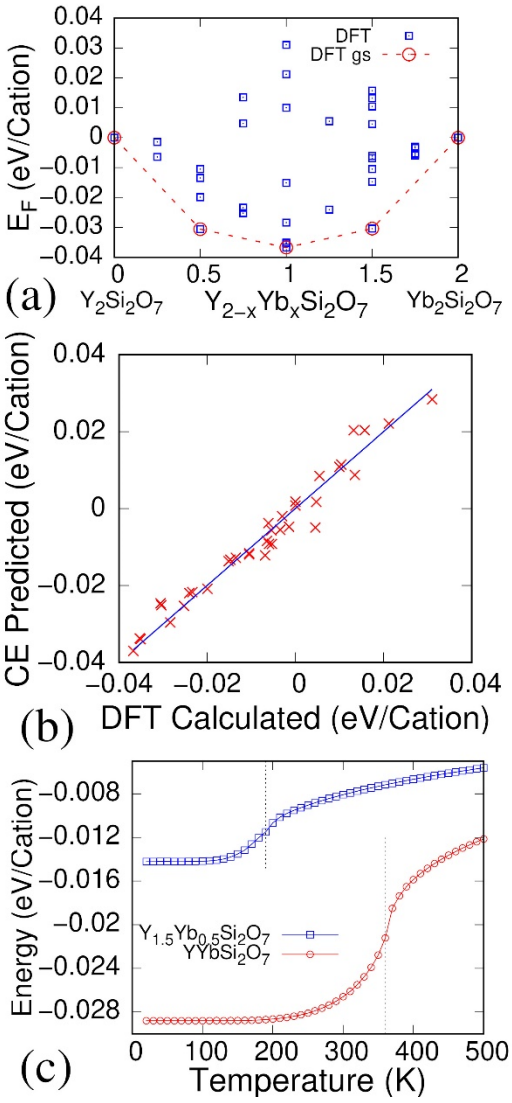

Figure 2 (a) The formation energy of mixing of $Y_2Si_2O_7$ and $Yb_2Si_2O_7$. The negative formation energy values suggest the structure is more favorable than the pure compounds of $Y_2Si_2O_7$ and $Yb_2Si_2O_7$. The red circles indicate ground state DFT calculated structures. (b) A comparison of DFT calculated energy and cluster expansion energy. (c) The energy profile of $YYbSi_2O_7$ and $Y_{3/2}Yb_{1/2}Si_2O_7$ as a function of temperature by Monte Carlo simulations to identify the order-disorder transition temperature. Note that the order-disorder transition temperature of $Y_{1/2}Yb_{3/2}Si_2O_7$ is the same as $Y_{3/2}Yb_{1/2}Si_2O_7$ due to the same formation energy relative to $Y_2Si_2O_7$ and $Yb_2Si_2O_7$ and not thus shown in the Figure (c).

3.2 Mechanical Properties

The elastic constants are referred to as an orthonormal coordinate system (*x, y, z*). The orthonormal axes are related to the monoclinic crystal lattice vectors (*a, b, c*) in the following way: *y*-axis is parallel to *b*-axis, *z*-axis is parallel to *c*-axis, and *x*-axis is perpendicular to *yz* plane. For the monoclinic system, the first six strains define the diagonal elastic constants C_{ii},

whereas the other strains give linear combinations of off-diagonal C_{ij}. The number of independent linear equations equals the number of unknown elastic moduli resulting in a well-defined system of equations that can be easily solved. By solving the linear equations for the C_{ij}, we obtained the elastic properties data in Table 1. In this context, all elastic constants have been examined by the corresponding stability criteria listed in the calculation section. All results satisfy the mechanical stability criteria, suggesting that all six material systems are mechanically stable with respect to all 13 strains.

As can be seen in Table 1, for the β phases of $Y_2Si_2O_7$ and $Yb_2Si_2O_7$, all elastic constants C_{ij} including both diagonal and off-diagonal components are very close to each other due to the same crystal structure. For the solid solution $YYbSi_2O_7$, the elastic constants are almost all lower than the pure cases of $Y_2Si_2O_7$ and $Yb_2Si_2O_7$ due to the mixing Y and Yb. For example, C_{11} of $YybSi_2O_7$ is 258.4 GPa compared with the corresponding C_{11} of 272.6 GPa for $Y_2Si_2O_7$, and 298.8 GPa for $Yb_2Si_2O_7$. For $Er_{1/4}Lu_{1/4}Y_{3/4}Yb_{3/4}Si_2O_7$, $Er_{1/2}Lu_{1/2}Y_{1/2}Yb_{1/2}Si_2O_7$, and $La_{1/4}Ce_{1/4}Er_{1/4}Lu_{1/4}Y_{1/2}Yb_{1/2}Si_2O_7$, their elastic constants deviate from those of pure cases of $Y_2Si_2O_7$, $Yb_2Si_2O_7$, and their mixture $YYbSi_2O_7$, even though all rare earth atoms occupied the Y cation site. For example, the C_{11} of the three solid solutions are respectively 201.5, 201.7, and 173.8 GPa, which are all noticeably lower than the pure cases 272.6 GPa ($Y_2Si_2O_7$) and 298.8 GPa ($Yb_2Si_2O_7$). However, the C_{33} of the three solid solutions as listed in Table 1 (247.7, 277.0, and 268.8 GPa) are all much higher than those of C_{33} 184.9 GPa ($Y_2Si_2O_7$), 215.5 GPa ($Yb_2Si_2O_7$), and 183.6 GPa ($YYbSi_2O_7$).

Table 1 The lattice parameters, elastic constants, and mechanical properties at 0 K for materials of $Y_2Si_2O_7$, $Yb_2Si_2O_7$, $YYbSi_2O_7$, $Er_{1/4}Lu_{1/4}Y_{3/4}Yb_{3/4}Si_2O_7$, $Er_{1/2}Lu_{1/2}Y_{1/2}Yb_{1/2}Si_2O_7$, and $La_{1/4}Ce_{1/4}Er_{1/4}Lu_{1/4}Y_{1/2}Yb_{1/2}Si_2O_7$. All values for elastic constants and mechanical properties are in the unit of GPa except Poisson's ratio, which is unitless. The values in parenthesis are reported experimental results.

	$Y_2Si_2O_7$	$Yb_2Si_2O_7$	$YYbSi_2O_7$	$Er_{1/4}Lu_{1/4}Y_{3/4}Yb_{3/4}$	$Er_{1/2}Lu_{1/2}Y_{1/2}Yb_{1/2}$	$La_{1/4}Ce_{1/4}Er_{1/4}Lu_{1/4}Y_{1/2}Yb_{1/2}$
a, b, c (Å)	6.88, 8.98, 4.72 (6.87, 8.96, 4.72)[a]	6.82, 9.01, 4.76 (6.80, 8.88, 4.71)[b]	6.76, 9.39, 4.45	6.77, 9.03, 4.75	6.75, 8.96, 4.77	6.89, 8.96, 4.72
α, β, γ (°)	90, 101.61,90 (90, 101.73, 90)[a]	90, 101.48, 90 (90, 101.98, 90)[b]	90, 101.39, 90	90, 100.8, 90	90, 98.13, 89.96	89.9, 99.1, 89.8
C_{11}	272.6	298.8	258.4	201.5	201.7	173.8
C_{22}	190.8	209.4	184.6	226.1	204.1	178.5
C_{33}	184.9	215.5	183.6	247.7	277.0	268.8
C_{44}	75.5	85.9	75.4	67.5	65.8	58.1
C_{55}	77.2	86.9	75.1	85.2	93.4	85.7

C_{66}		52.2	57.6	49.4	10.4	71.7	57.8
C_{12}		78.4	91.4	74.4	106.4	101.7	86.9
C_{13}		96.9	110.6	91.8	110.4	115.5	104.4
C_{23}		107.4	121.7	99.9	107.2	104.7	92.9
C_{15}		-15.3	-17.3	-14.3	-4.2	-5.1	-1.5
C_{25}		32.4	36.6	25.5	0.2	39.1	-18.4
C_{35}		13.8	13.5	8.53	17.5	-16.6	13.7
C_{46}		20.2	22.5	15.5	-9.9	26.1	-5.8
Bulk Modulus	Voigt	134.9	152.4	128.7	147.0	147.4	132.2
	Reuss	130.2	147.3	125.8	141.1	142.4	125.7
	Hill	132.5	149.8	127.3	144.1	144.9	128.9
Young's Modulus	Voigt	168.8	188.4	164.7	180.8	181.8	162.6
	Reuss	145.7	162.7	147.3	154.8	155.7	143.1
	Hill	157.3(170)[c]	175.6(162)[c]	156.1	167.9	168.9	152.9
Shear Modulus	Voigt	65.4	72.8	64.0	69.8	70.2	62.8
	Reuss	55.5	61.8	56.4	58.8	59.1	54.6
	Hill	60.4(65)[c]	67.3(62)[c]	60.2	64.3	64.7	58.7
Poisson's ratio	Voigt	0.29	0.29	0.29	0.30	0.29	0.30
	Reuss	0.31	0.32	0.31	0.32	0.32	0.31
	Hill	0.30(0.32)[c]	0.31(0.31)[c]	0.30	0.31	0.31	0.30
Vickers Hardness	Voigt	6.83	7.29	7.00	6.97	7.05	6.38
	Reuss	4.69	5.04	5.24	4.74	4.73	4.79
	Hill	5.74	6.15	6.11	5.84	5.87	5.58

[a]: Ref.[26]. [b]. Ref.[27]. [c]. Ref.[28]

We evaluated the average bulk elastic properties using the Voigt-Reuss-Hill methods and collected all entries in the lower panel of Table 1. Generally, the bulk modulus is a special elastic constant that is related to the measure of resistance to volume change by applied pressure. As shown in Table 1, the bulk moduli for the β phases of $Y_2Si_2O_7$ from Voigt, Reuss, and Hill schemes are very close (ranging from 134.9 to 130.2 GPa), implying reliable results of the elastic constants [29]. Moreover, the calculated shear modulus of $Yb_2Si_2O_7$ (67.3 GPa) and $Y_2Si_2O_7$ (60.4 GPa) are in good agreement with experimental results $Yb_2Si_2O_7$ (62 GPa) and $Y_2Si_2O_7$ (65 GPa) [3]. Calculated average bulk modulus, Young's modulus, and shear modulus exhibit the same trend as the single crystal elastic constants among the six material systems. β $Yb_2Si_2O_7$ has higher bulk modulus, Young's modulus, and shear modulus than β $Y_2Si_2O_7$. However, the average elastic moduli of $YYbSi_2O_7$ are all lower than ROM estimates.

For $Er_{1/4}Lu_{1/4}Y_{3/4}Yb_{3/4}Si_2O_7$ and $Er_{1/2}Lu_{1/2}Y_{1/2}Yb_{1/2}Si_2O_7$, the bulk moduli lie between the pure cases of $Y_2Si_2O_7$, $Yb_2Si_2O_7$, and higher than the mixing material $YYbSi_2O_7$. For example, the bulk moduli of the two solid solutions are respectively 144.1 and 144.9 GPa, which fall in the pure cases 132.5 GPa ($Y_2Si_2O_7$) and 149.8 GPa ($Yb_2Si_2O_7$). The Young's modulus and shear modulus can be used to estimate the stiffness of materials upon tensile and shear pressure. The

Young's modulus and shear modulus of $Er_{1/4}Lu_{1/4}Y_{3/4}Yb_{3/4}Si_2O_7$ and $Er_{1/2}Lu_{1/2}Y_{1/2}Yb_{1/2}Si_2O_7$ also exhibit a similar trend with an intermediate value between the pure cases of $Y_2Si_2O_7$ and $Yb_2Si_2O_7$, but higher than the mixing material $YYbSi_2O_7$ and $La_{1/4}Ce_{1/4}Er_{1/4}Lu_{1/4}Y_{1/2}Yb_{1/2}Si_2O_7$, which means that the Er and Lu addition still maintain relatively strong resistance to deformations upon tensile and shear stress. From mechanical property point of view, the four rare earth elements alloyed solid solution systems are all mechanically stable with reasonable intermediate moduli values between the pure cases of $Y_2Si_2O_7$ and $Yb_2Si_2O_7$.

In addition to thermal and environmental properties, higher ductility or toughness is very desirable for T/EBC to resist against crack initiation and propagation. However, oxides are intrinsically brittle due to ionic bonding and hence have low fracture toughness. Modeling ductility or toughness of oxides is extremely challenging. Popular ductility criteria in solids include: The ratio of bulk modulus and shear modulus [30], D-parameter [31], and shear instability [32]. Toughness of metals and ceramics is reported to increase with B/G ratio although the ratio of minimum affine shear energy over tensile strain energy correlates better with toughness than B/G ratio [33]. The B/G ratio also determines the Poisson's ratio (ν) that reflects the way structural elements are packed and provides information about the characteristics of the bonding forces and chemical bonding [34]. In the present work, the calculated B/G values of six systems are similar: 2.19 ($Y_2Si_2O_7$), 2.22 ($Yb_2Si_2O_7$), 2.11 ($YybSi_2O_7$), 2.24 ($Er_{1/4}Lu_{1/4}Y_{3/4}Yb_{3/4}Si_2O_7$), 2.24 ($Er_{1/2}Lu_{1/2}Y_{1/2}Yb_{1/2}Si_2O_7$), and 2.20 ($La_{1/4}Ce_{1/4}Er_{1/4}Lu_{1/4}Y_{1/2}Yb_{1/2}Si_2O_7$). While the calculated B/G ratios are well above the critical threshold 1.75, this does not necessarily mean that these oxides are ductile. To the contrary, the value of Young's moduli E shown in Fig. 7 are noticeably higher than corresponding B, suggesting a lack of ductility of these oxides. . Hardness is another important mechanical property defined as the resistance of a material to deformation and may be predicted using macroscopic and microscopic models. In this work, we use the semi-empirical equations of hardness proposed by ref. [35] to estimate the hardness $H_V = 1.887\left(\frac{G^3}{B^2}\right)^{0.585} - 3$.

Based on the elastic constants at 0 K determined by the strain-energy methods, the temperature effects on the elastic constants can be evaluated by considering the corresponding free energies for the three phases. Figure 3(a, c, e, g, i, and k) show that the diagonal elements of elastic constants for $Y_2Si_2O_7$, $Yb_2Si_2O_7$, $YYbSi_2O_7$, $Er_{1/4}Lu_{1/4}Y_{3/4}Yb_{3/4}Si_2O_7$,

$Er_{1/2}Lu_{1/2}Y_{1/2}Yb_{1/2}Si_2O_7$, and $La_{1/4}Ce_{1/4}Er_{1/4}Lu_{1/4}Y_{1/2}Yb_{1/2}Si_2O_7$ systems exhibit pronounced softening with temperature. The softening elastic constants with different slopes to the temperature reflect the anisotropic responses to the external pressure. Solved by the linear equations based on the results of diagonal components, it is not surprising to see that the off-diagonal components of elastic constants in Figure 3(b, d, f, h, j, and l) display a certain extent of hardening with temperature due to different slopes of the diagonal components. Similar to the elastic constants, the mechanical moduli including bulk modulus, Young's modulus and shear modulus depicted in Figure 4 also exhibit thermal softening upon temperature increases.

The elastic constants offer an intriguing opportunity for investigating elastic anisotropy, which plays a crucial role in the formation of microcracks within coatings. Specifically, the direction with a high modulus corresponds to a direction with high fracture energy, while the direction with a low modulus corresponds to a direction with low fracture energy. Understanding the anisotropy of elastic properties provides valuable insights into predicting the directions with low and high fracture energy within the crystal. Figure 5 visually demonstrates the pronounced anisotropic nature of Young's and shear moduli for all systems. In the case of $Y_2Si_2O_7$, $Yb_2Si_2O_7$, and $YYbSi_2O_7$, their Young's and shear moduli exhibit very similar anisotropy properties. The highest Young's moduli, shown in Figure 5(a, c, e), are approximately 180 GPa in the (100) plane, 250-270 GPa in the (010) plane, and 205 GPa in the (001) plane. Similarly, the lowest Young's moduli are approximately 120 GPa in all three systems and in all three planes. Likewise, the highest and lowest Young's moduli of the $Er_{1/4}Lu_{1/4}Y_{3/4}Yb_{3/4}Si_2O_7$, $Er_{1/2}Lu_{1/2}Y_{1/2}Yb_{1/2}Si_2O_7$, and $La_{1/4}Ce_{1/4}Er_{1/4}Lu_{1/4}Y_{1/2}Yb_{1/2}Si_2O_7$ systems are very close to those of the $Y_2Si_2O_7$, $Yb_2Si_2O_7$, and $YYbSi_2O_7$ systems. Turning to the shear modulus anisotropy property, all six systems, as depicted in Figure 5(b, d), exhibit a very similar shape in the (100) and (010) planes. However, for the $La_{1/4}Ce_{1/4}Er_{1/4}Lu_{1/4}Y_{1/2}Yb_{1/2}Si_2O_7$ system, the shear modulus in the (001) plane differs considerably from all other systems. This discrepancy might be attributed to the instability of the addition of $La_2Si_2O_7$ and $Ce_2Si_2O_7$ in the monoclinic β phase. Notably, the shear modulus varies significantly along different slip directions in all three planes, indicating a strong variation in resistance to shear deformation.

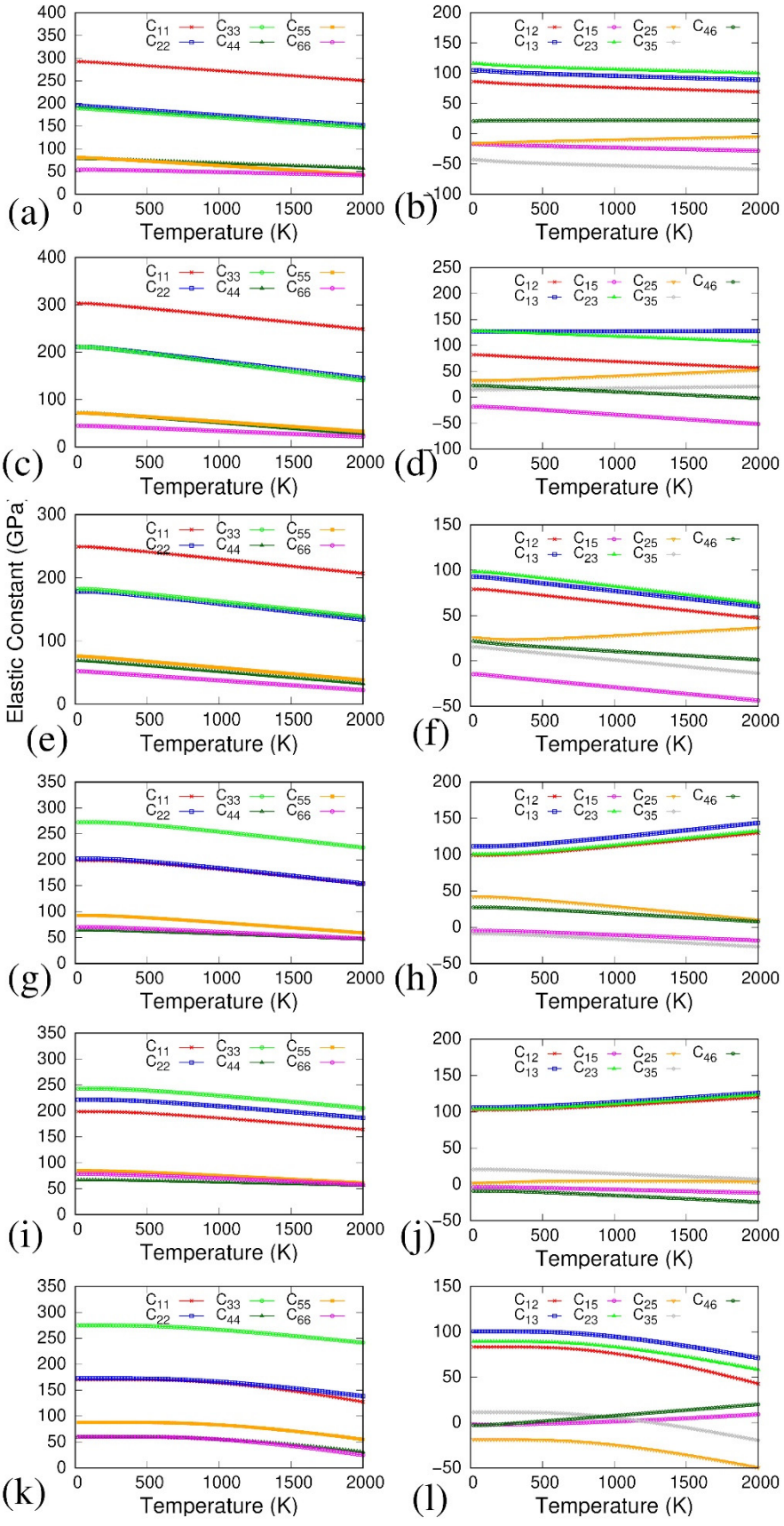
(a)
(b)
(c)
(d)
(e)
(f)
(g)
(h)
(i)
(j)
(k)
(l)
Elastic Constant (GPa)
Temperature (K)
C11 C22 C33 C44 C55 C66
C12 C13 C15 C23 C25 C35 C46

Figure 1 *The temperature-dependent elastic constants for the six systems of (a, b) $Y_2Si_2O_7$, (c, d) $Yb_2Si_2O_7$, (e, f) $YYbSi_2O_7$, (g, h) $Er_{1/2}Lu_{1/2}Y_{1/2}Yb_{1/2}Si_2O_7$, (i, j) $Er_{1/4}Lu_{1/4}Y_{3/4}Yb_{3/4}Si_2O_7$, and (k,l) $La_{1/4}Ce_{1/4}Er_{1/4}Lu_{1/4}Y_{1/2}Yb_{1/2}Si_2O_7$.*

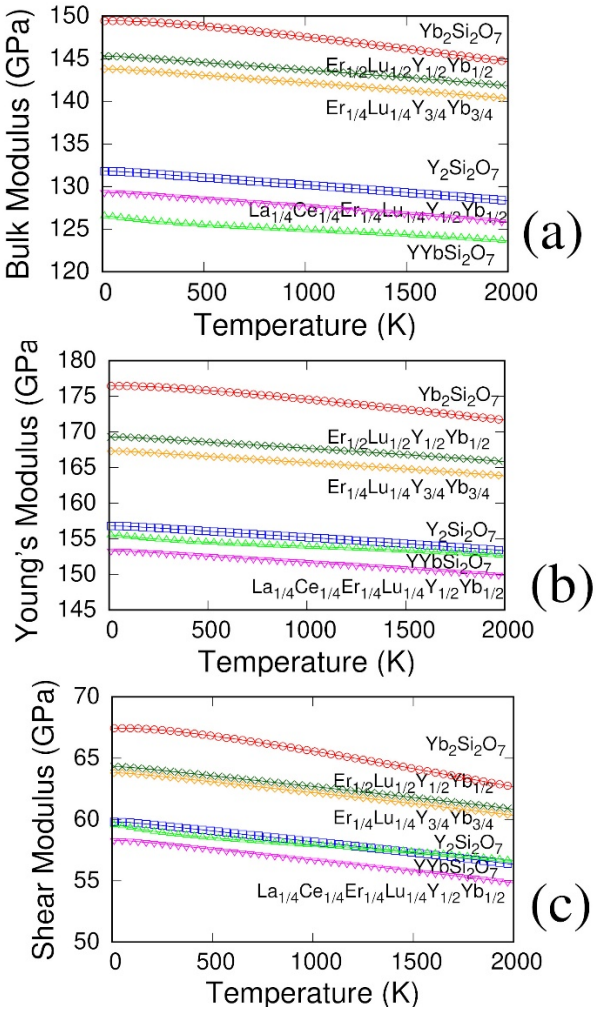

Figure 4 *The temperature-dependent (a) bulk moduli, (b) Young's moduli, and (c) shear moduli for the six systems of $Y_2Si_2O_7$, $Yb_2Si_2O_7$, $YYbSi_2O_7$, $Er_{1/2}Lu_{1/2}Y_{1/2}Yb_{1/2}Si_2O_7$, $Er_{1/4}Lu_{1/4}Y_{3/4}Yb_{3/4}Si_2O_7$, and $La_{1/4}Ce_{1/4}Er_{1/4}Lu_{1/4}Y_{1/2}Yb_{1/2}Si_2O_7$.*

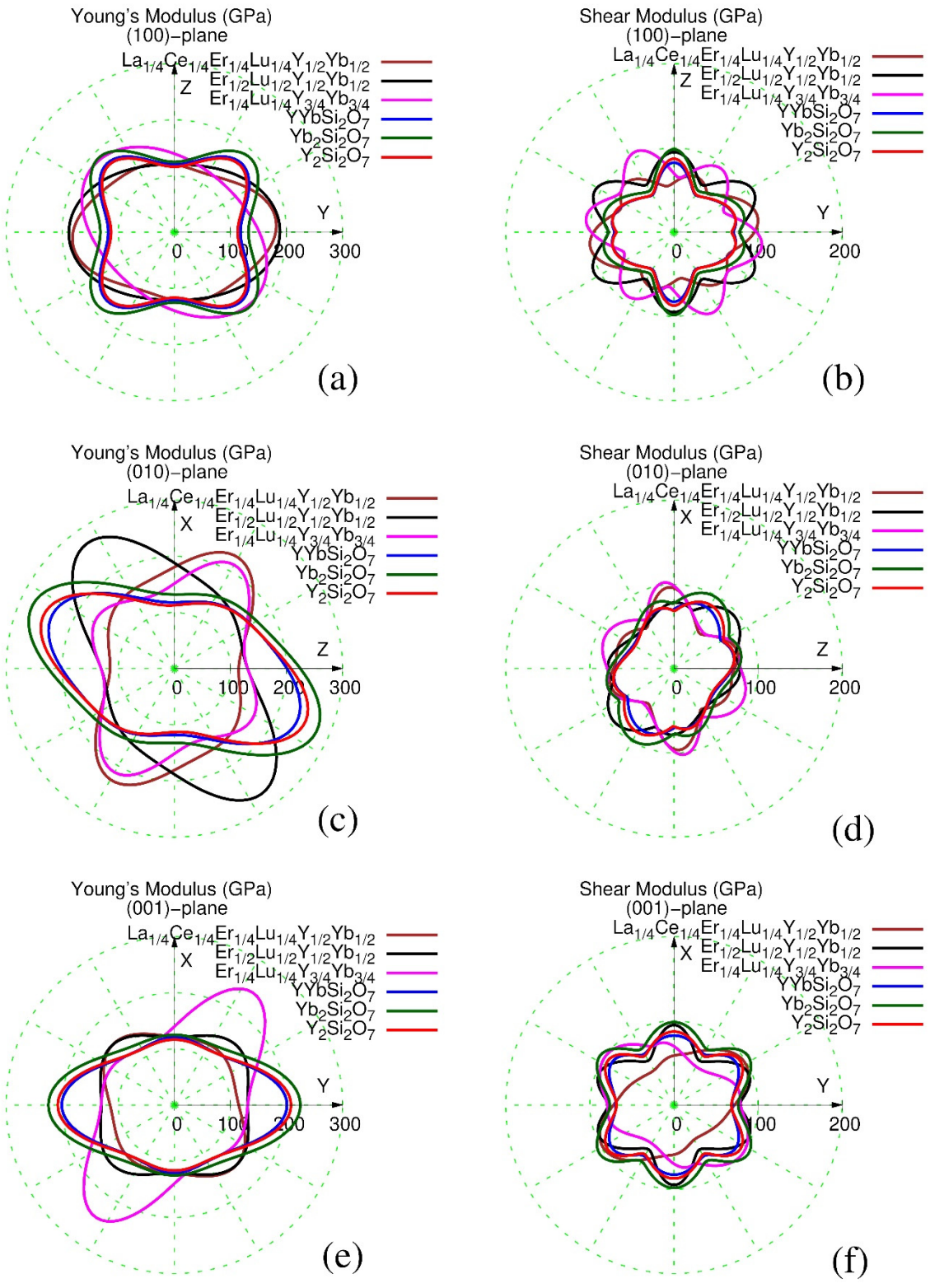

Figure 5 *Elastic anisotropy of Young's modulus and shear modulus in different plane of (a-b) (100), (c-d) (010), and (e-f) (001), respectively.*

3.3 Phonon Dispersion

Having established the elastic constants and mechanical properties of six systems by the strain-energy methods together with Debye model for temperature effects, we now turn our attention to the thermal properties including CTE and lattice thermal conductivities. The very first step to investigate the thermal property is the lattice vibration characterization by phonon dispersion along the high symmetrical lines in the Brillouin zone. It can be observed from phonon dispersions (Figure 6) that our calculation results do not show any phonon branch with imaginary frequencies at any points in the reciprocal space. Therefore, we can safely conclude that all six phases including the solid solutions are dynamically stable at their equilibrium volumes.

To characterize the phonon dispersion behavior of these six systems, we compare the average values of the Debye temperature, phonon velocities, and Grüneisen parameters. By examining the phonon dispersion, the longitudinal Debye temperature can be calculated from $\Theta = \omega_D / k_B$ (ω_D is the largest acoustic frequency in each direction, and k_B is the Boltzmann constant). The average longitudinal Debye temperatures are found to be 155 K for $Y_2Si_2O_7$ and 89 K for $Yb_2Si_2O_7$. Compared with the pure cases, the longitudinal Debye temperatures for four solid solutions are 78 K ($YYbSi_2O_7$), 74 K ($Er_{1/4}Lu_{1/4}Y_{3/4}Yb_{3/4}Si_2O_7$), 72 K ($Er_{1/2}Lu_{1/2}Y_{1/2}Yb_{1/2}Si_2O_7$), and 69 K ($La_{1/4}Ce_{1/4}Er_{1/4}Lu_{1/4}Y_{1/2}Yb_{1/2}Si_2O_7$), respectively. Generally speaking, lower Debye temperatures imply lower lattice thermal conductivity. Hence the cation mixing in solid solutions decreases the longitudinal Debye temperatures and consequently lowers lattice thermal conductivity.

Similarly, the phonon velocities of acoustic branches v_i approximated by the long-wavelength limit of group velocities can be another physical quantity to explain lattice thermal conductivity behavior. Calculated by $v_m^{-1} = \left(\frac{1}{3}\sum_{i=1}^{3}\frac{1}{v_i^3}\right)^{\frac{1}{3}}$, the average phonon velocities for $Y_2Si_2O_7$ and $Yb_2Si_2O_7$ are 4950 and 3207 m/s, respectively. The average phonon velocities for $YYbSi_2O_7$, $Er_{1/4}Lu_{1/4}Y_{3/4}Yb_{3/4}Si_2O_7$, $Er_{1/2}Lu_{1/2}Y_{1/2}Yb_{1/2}Si_2O_7$, and $La_{1/4}Ce_{1/4}Er_{1/4}Lu_{1/4}Y_{1/2}Yb_{1/2}Si_2O_7$ are 3872, 4021, 3925, and 3726 m/s, respectively. The slower phonon velocity generally suggests relatively sluggish phonon transport and thus tends to lower lattice thermal conductivity.

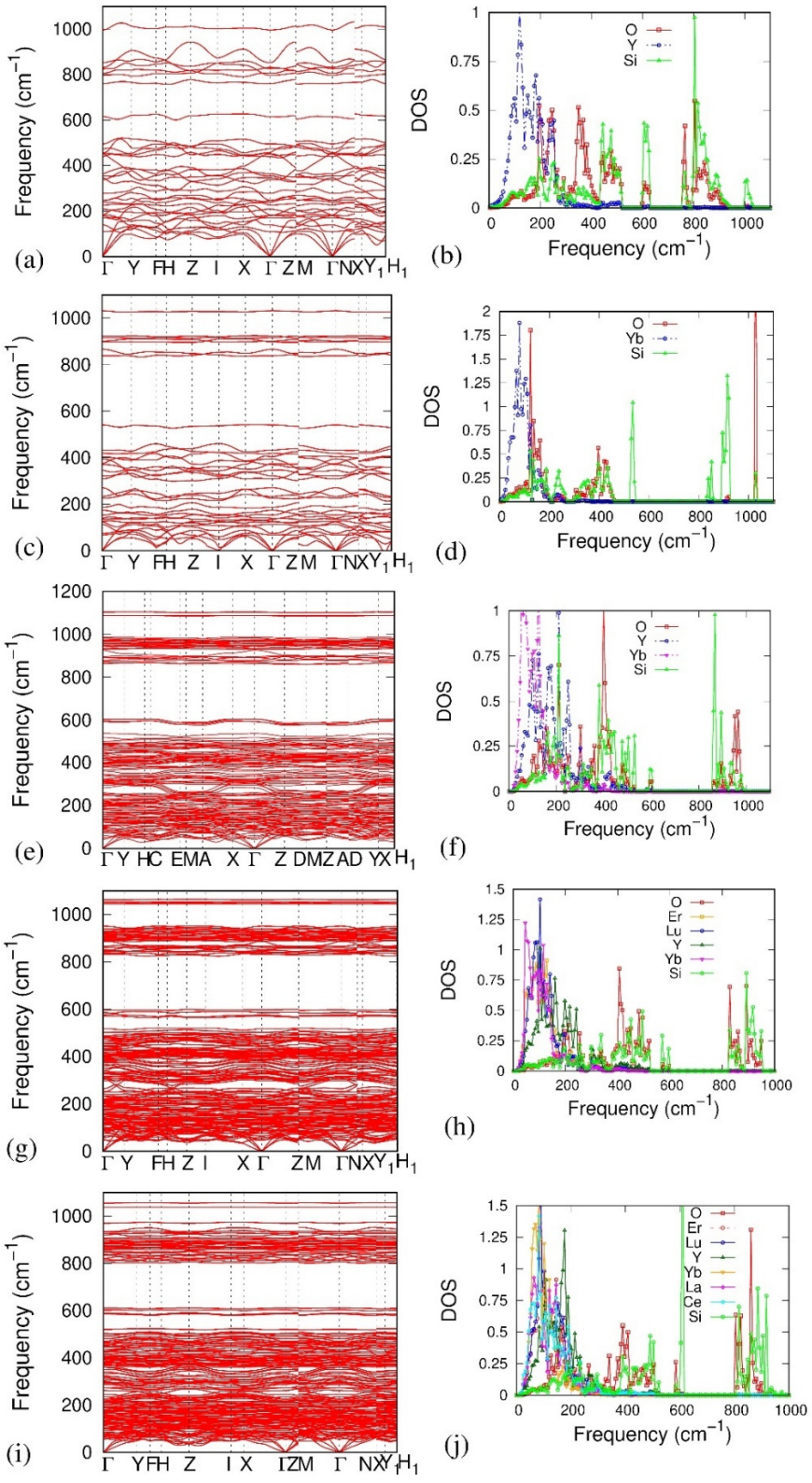
Frequency (cm^{-1})
DOS
Frequency (cm^{-1})
(a)
(b)
(c)
(d)
(e)
(f)
(g)
(h)
(i)
(j)
O
Y
Si
Yb
Er
Lu
La
Ce
Γ Y FH Z I X Γ ZM ΓNXY$_1$H$_1$
Γ Y HC EMA X Γ Z DMZAD YX H$_1$
Γ Y FH Z I X Γ ZM ΓNXY$_1$H$_1$
Γ YFH Z I X ΓZM Γ NXY$_1$H$_1$

Figure 6 *The phonon dispersion (a, c, e, g, i) and projected phonon density of states (b, d, f, h, j) at corresponding equilibrium volume V_0 for the five systems of (a, b) $Y_2Si_2O_7$, (c, d) $Yb_2Si_2O_7$, (e, f) $YYbSi_2O_7$, (g, h) $Er_{1/2}Lu_{1/2}Y_{1/2}Yb_{1/2}Si_2O_7$, and (i, j) $La_{1/4}Ce_{1/4}Er_{1/4}Lu_{1/4}Y_{1/2}Yb_{1/2}Si_2O_7$.*

The projected phonon density of states for the five systems illustrated in Figure 6(b, d, f, h, and j) show a similar behavior. It is not surprising to see that the most significant low frequency peaks are located within a low frequency range of 40-200 cm^{-1} due to the heaviest rare earth atomic mass in the cell. For the lightest species (oxygen), the local vibration modes are observed in all systems with the highest peak at approximately 1050 cm^{-1} for the $Yb_2Si_2O_7$ phase, the lowest at approximately 800 cm^{-1} for $Y_2Si_2O_7$, and others between 800 and 1050 cm^{-1}.

3.4 Coefficients of Thermal Expansion and Lattice Thermal Conductivities

Knowing the phonon dispersions within quasi-harmonic approximation at six different volumes for each system, we evaluated CTE that is derived from the volume with the minimized free energy as a function of temperature. To obtain the free energy, we integrated the phonon energy according to Equ. (9) in Section 2 over the lattice vibrational frequencies in the entire Brillouin zone with a converged dense mesh. The free energies of $Y_2Si_2O_7$ are plotted as a function of volume and temperature in Figure 7(a) as an example, while the free energies of other systems are not shown since the basic shapes are almost the same. Based on the volume at the minimum free energy as a function of temperature, the volumetric coefficients of thermal expansion are then derived. In order to compare our calculated results with the CTE values reported from experiments, we divided our calculated volumetric CTE values by 3 to obtain the apparent bulk coefficient of thermal expansion (ABCTE) [28, 36]. In such a way, we simplify the complex CTE tensor for anisotropic structures and make it much easier to compare with available data.

Figure 7(b) shows that the ABCTE of β-$RE_2Si_2O_7$ (RE=Y and Yb) and some rare earth solid solution disilicates at low temperatures (< 500 K) are generally small and quickly become saturated when temperature exceeds 500 K for all eight systems [28]. Clearly, the ABCTE of $Y_2Si_2O_7$ is the lowest among the eight systems with an average value of 3.5×10^{-6} K^{-1} over a temperature range of 500 to 2000 K. $Yb_2Si_2O_7$ has higher average ABCTE (4.2×10^{-6} K^{-1}) than $Y_2Si_2O_7$ due to Yb-attributed relative low frequencies, which consequently induce relatively high-vibrational entropy. Our calculated ABCTE values agree very well with experimental measurements of 3.6-4.5×10^{-6} K^{-1} for both $Yb_2Si_2O_7$ and $Yb_2Si_2O_7$ [28]. As expected, the

ABCTE of the solid solution of $YYbSi_2O_7$ lies between that of $Y_2Si_2O_7$ and $Yb_2Si_2O_7$. The average ABCTE values of $Er_{1/2}Lu_{1/2}Y_{1/2}Yb_{1/2}Si_2O_7$ (5.2×10^{-6} K^{-1}) and $Er_{1/4}Lu_{1/4}Y_{3/4}Yb_{3/4}Si_2O_7$ (5.1×10^{-6} K^{-1}) fall in a desired range of CTE closely matching with SiC. The largest CTE among the eight systems is $La_{1/4}Ce_{1/4}Er_{1/4}Lu_{1/4}Y_{1/2}Yb_{1/2}Si_2O_7$, with an average value of approximately 7.9×10^{-6} K^{-1} over a temperature range of 500 to 2000 K. Since both A and G phases of $La_2Si_2O_7$ and $Ce_2Si_2O_7$ have relatively high ABCTE, ranging from approximately 6×10^{-6} K^{-1} to 14×10^{-6} K^{-1} [3], it is not surprising that adding La and Ce to β $RE_2Si_2O_7$ noticeably increases CTE as seen in $La_{1/4}Ce_{1/4}Er_{1/4}Lu_{1/4}Y_{1/2}Yb_{1/2}Si_2O_7$. From a thermal expansion point of view, the good candidates with desired CTE value matching with SiC are β-$Yb_2Si_2O_7$ (4.2×10^{-6} K^{-1}), solid solutions of $YYbSi_2O_7$ (4.0×10^{-6} K^{-1}), $Er_{1/2}Lu_{1/2}Y_{1/2}Yb_{1/2}Si_2O_7$ (5.2×10^{-6} K^{-1}), and $Er_{1/4}Lu_{1/4}Y_{3/4}Yb_{3/4}Si_2O_7$ (5.1×10^{-6} K^{-1}).

The calculated lattice thermal conductivities for six systems are depicted in Figure 7(c). It is evident that the thermal conductivities of pure $Yb_2Si_2O_7$ are lower than those of pure $Y_2Si_2O_7$. The physical origins of the lower thermal conductivity of $Yb_2Si_2O_7$ are analyzed in the phonon dispersion section, namely, slow phonon group velocities, low longitudinal Debye temperatures, and relative high lattice anharmonicity characterized by higher Grüneisen parameters. We found that our calculated results are slightly higher than the experimental measurements for pure $Y_2Si_2O_7$ and $Yb_2Si_2O_7$. For example, the calculated values 6.1 and 4.2 W/m/K at 300 K are higher than experimental values 5.5 and 4.1 W/m/K for $Y_2Si_2O_7$ and $Yb_2Si_2O_7$, respectively [3]. The reason for these small discrepancies is likely because only the most important three-phonon processes are considered herein, whereas additional phonon transport events such as impurity scattering, grain boundary scattering, etc., will also contribute to decreasing the thermal conductivity in real materials.

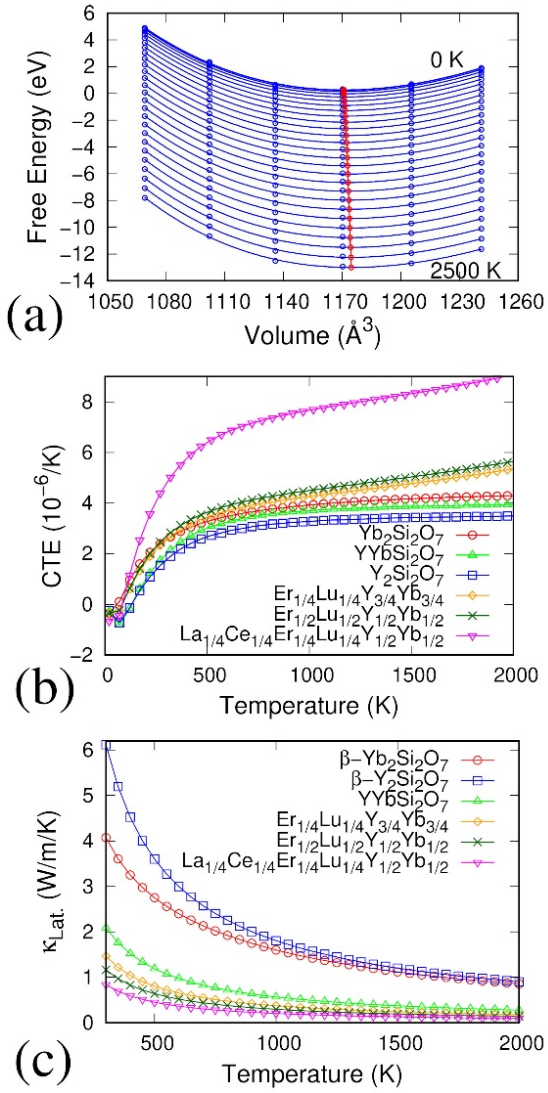

Figure 7 *(a) An example of Helmholtz free energy as a function of volume and temperature for $Y_2Si_2O_7$ system. The blue dots and blue lines are respectively DFT calculated values and fitted results. The red dots represent the minimum free energy at corresponding volume and temperatures ranging from 0 to 2500 K with a step of 100 K. A comparison of the thermal properties as a function of temperature including (b) apparent bulk coefficients of thermal expansion and (c) lattice thermal conductivity of six systems.*

Beyond $Y_2Si_2O_7$ and $Yb_2Si_2O_7$, the lattice thermal conductivities of the other four solid solution systems are all lower than those of the two pure cases. The lowered lattice thermal conductivities of solid solutions are attributed to the atomic mass fluctuation among different atomic species of Y (88.9), La (138.9), Ce (140.1), Er (167.3), Yb (173.1), and Lu (175.0). For example, the atomic mass of Y is approximately half that of Yb in $YYbSi_2O_7$ system, inducing

strong phonon scattering centers due to the mass difference in the cation site. However, the random distribution of the different rare earth species with different atomic size and electronegativity causes strong lattice distortion not only in the cation site but also in the entire lattice, which explains the trend that the higher the number of distinct cation species, the lower the thermal conductivity. From thermal conductivity point of view, the good candidate thermal barrier materials are $YYbSi_2O_7$ (0.35 W/m/K at 1500K), $Er_{1/4}Lu_{1/4}Y_{3/4}Yb_{3/4}Si_2O_7$ (0.23 W/m/K at 1500 K), $Er_{1/2}Lu_{1/2}Y_{1/2}Yb_{1/2}Si_2O_7$ (0.19 W/m/K at 1500 K), and $La_{1/4}Ce_{1/4}Er_{1/4}Lu_{1/4}Y_{1/2}Yb_{1/2}Si_2O_7$ (0.16 W/m/K at 1500 K).

4. Discussion

Knowledge of the mechanical and thermal properties of components can be utilized to formulate design rules for high-entropy materials as the properties of multi-component phases generally follow ROM. ROM is commonly used to predict various properties of multi-component materials, providing a rough guide for estimating properties such as elastic modulus, CTE, and lattice thermal conductivity. To make a connection of our calculated physical properties, we investigate the relationship between rare earth ionic radius and DFT calculated properties by a Pearson correlation analysis and a normalized root-mean-square relative deviation. The Pearson correlation parameter *r* between two variables, X and Y, is calculated as:

$$r = \frac{\Sigma_{i=1}^{n}(X_i-\bar{X})(Y_i-\bar{Y})}{\sqrt{\sum_{i=1}^{n}(X_i-\bar{X})^2}\sqrt{\sum_{i=1}^{n}(Y_i-\bar{Y})^2}} \quad (12)$$

where $\bar{X}$ and $\bar{Y}$ are the mean values of *X* and *Y*. The Pearson correlation parameter ranges from -1 to 1 and encompassed both positive and negative correlations. The closer the magnitudes to 1 (or -1), the stronger the correlation, while values closer to zero suggest a weaker correlation. A negative correlation indicates that when one variable increases, the other variable decreases. The normalized root-mean-square relative deviation (RMSD) was used to quantify the discrepancy between DFT-predicted quantities (Y_i) and the average value ($\bar{Y}$) estimated from ROM (Eq. (13)). Lower values of RMSD indicate better agreement between the compared data sets.

$$RMSD = \sqrt{\frac{\sum_{i=1}^{n}(Y_i-\bar{Y})^2}{(N-1)\sum_{i=1}^{n}(\bar{Y})^2}} \quad (13)$$

As shown in Figure 8, the bulk, Young's, and shear moduli values from Hill scheme are taken as examples to demonstrate the relationship with rare earth ionic radius. Generally, the moduli decrease as the rare earth ionic radius increases. The Pearson correlations of the three moduli are -0.76, -0.71, and -0.89, respectively, suggesting that adding rare earth ions of large radius induces a decrease in the moduli. The calculated RMSD of the moduli is as small as 0.068, 0.057, and 0.053, indicating good agreement between the data sets being compared. The apparent bulk coefficient of thermal expansion (ABCTE) exhibits a relative strong positive correlation of 0.68. The strong negative correlation of moduli suggests that the rare-earth metal-oxide bond strength decreases with increasing ionic radius. Consequently, the weakening bond strength with rare earth ionic radius also suggests a large coefficient of thermal expansion. The mechanical properties trend with RE radius also agrees with the ABCTE trend. However, the magnitude of ABCTE correlation (|0.68|) is slightly lower than the magnitude of moduli correlations (|0.76|, |0.71|, |0.89|) due to the configurational entropy contribution to the mixing of rare earth cation site.

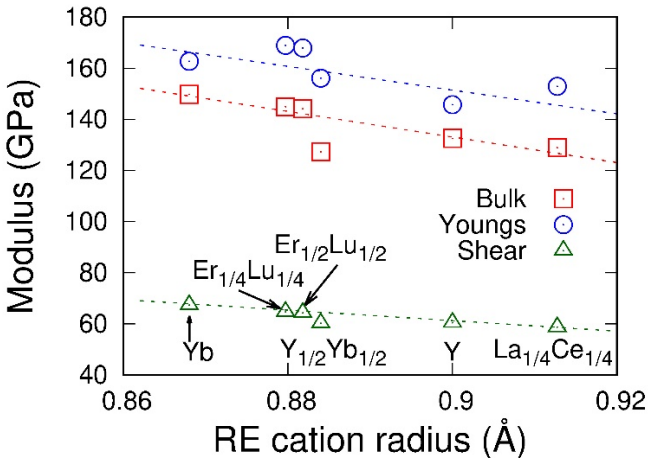

Figure 8 *The calculated mechanical modulus in Hill scheme as a function of rare earth cation radius. The rare earth labels Yb, $Er_{1/4}Lu_{1/4}$, $Er_{1/2}Lu_{1/2}$, $Y_{1/2}Yb_{1/2}$, Y, and $La_{1/4}Ce_{1/4}$ at corresponding average cation radius respectively represent β-$Yb_2Si_2O_7$, solid solutions of $Er_{1/4}Lu_{1/4}Y_{3/4}Yb_{3/4}Si_2O_7$, $Er_{1/2}Lu_{1/2}Y_{1/2}Yb_{1/2}Si_2O_7$, $YYbSi_2O_7$, β-$Y_2Si_2O_7$, and $La_{1/4}Ce_{1/4}Er_{1/4}Lu_{1/4}Y_{1/2}Yb_{1/2}Si_2O_7$.*

In contrast, using the lattice thermal conductivity results at 1000 K as shown in Figure 7(c), we get a weak negative correlation of thermal conductivity with rare earth ionic radius of -0.21. The presence of a weak correlation suggests that the impact of the rare earth ionic radius effect is

overshadowed by the high entropy effect induced by the configurational disorder of interatomic force constants. This disorder leads to an increase in phonon scattering, which in turn results in reduced lattice thermal conductivity. In comparison to the elastic moduli and ABCTE, the lattice thermal conductivity of multi-component systems is generally significantly lower than what would be predicted by the rule of mixtures. This result agrees with observations for other high entropy materials [28] and is likely due to the configurational disorder in the interatomic force constants.

5. Summary

In the present study we utilize DFT methods together with combinatorial chemistry methodology to design multifunctional high-entropy β-$RE_2Si_2O_7$ systems for desired CTE matching SiC and lower lattice thermal conductivity than $Yb_2Si_2O_7$. Due to the exact same atomic structure of β-$Y_2Si_2O_7$ and β-$Yb_2Si_2O_7$ with very similar lattice parameters, our cluster expansion calculations and Monte Carlo simulations predict that the β-$YYbSi_2O_7$ phase is thermodynamically stable at room temperature and undergoes an order-disorder transition at 360 K, agreeing with experiments [22].

Based on the DFT-predicted mechanical and thermal property results, various systems emerge as promising candidates for next-generation T/EBC to protect SiC-based ceramic matrix composites. The most cost-effective system is $YYbSi_2O_7$ with a significantly decreased lattice thermal conductivity, acceptable CTE values, and elastic properties similar to pure $Y_2Si_2O_7$ and $Yb_2Si_2O_7$. Alternatively, $Er_{1/4}Lu_{1/4}Y_{3/4}Yb_{3/4}Si_2O_7$ or $Er_{1/2}Lu_{1/2}Y_{1/2}Yb_{1/2}Si_2O_7$, or concentration-gradient coating layers between these two compositions, offer even lower lattice thermal conductivities that approach the limit of amorphous solids at high temperatures, while maintaining CTE within a small range of SiC. The mechanical properties of these systems likewise fall between those of pure $Y_2Si_2O_7$ and $Yb_2Si_2O_7$, and both are mechanically stable. In summary, this article not only predicts new $RE_2Si_2O_7$ T/EBC materials that are thermodynamically and mechanically stable with ultralow lattice thermal conductivity superior to $Yb_2Si_2O_7$ but also proposes an important computational material design methodology for rapid novel material discovery with attractive multi-functional and mechanical properties for extreme environment applications such as hydrogen gas turbine technologies.

Acknowledgments

This work was performed in support of the U.S. Department of Energy's (DOE) Fossil Energy and Carbon Management Advanced Energy Materials Research Program. The research was executed through the National Energy Technology Laboratory's (NETL) Research and Innovation Centers Advanced Materials Development Field Work Proposal. This research used resources of the National Energy Research Scientific Computing Center (NERSC), a DOE Office of Science User Facility supported by the Office of Science under Contract No. DE-AC02-05CH11231 using NERSC award ALCC-ERCAP0022624.

Disclaimer

References

[1] N.P. Padture, M. Gell, E. H. Jordan, Thermal Barrier Coatings for Gas-Turbine Engine Applications, Science 296 (2002) 280-284.
[2] N.P. Padture, Advanced structural ceramics in aerospace propulsion, Nature Materials 15 (2016) 804-809.
[3] L.R. Turcer, N. P. Padture, Towards multifunctional thermal environmental barrier coatings (TEBCs) based on rare-earth pyrosilicate solid-solution ceramics, Scripta Materialia 154 (2018) 111-117.
[4] D. Tejero-Martin, C. Bennett, T. Hussain A review on environmental barrier coatings: History, current state of the art and future developments, Journal of the European Ceramic Society 41 (2021) 1747-1768.
[5] K.N. Lee, $Yb_2Si_2O_7$ Environmental barrier coatings with reduced bond coat oxidation rates via chemical modifications for long life, Journal of the American Ceramic Society 102 (2019) 1507-1521.
[6] Z. Chen, C. Lin, W. Zheng, Y. Zeng, Y. Niu, Investigation on improving corrosion resistance of rare earth pyrosilicates by high-entropy design with RE-doping, Corrosion Science 199 (2022) 110217.
[7] G. Kresse, and J. Furthmuller, Efficient iterative schemes for ab initio total-energy calculations using a plane-wave basis set, Phys. Rev. B 54 (1996) 11169-11186.

[8] P.E. Blochl, Projector augmented-wave method, Phys. Rev. B: Condens. Matter Mater. Phys. 50 (1994) 17953-17979.
[9] J.P. Perdew, K. Burke, and M. Ernzerhof, Generalized Gradient Approximation Made Simple, Phys. Rev. Lett. 77 (1996) 3865.
[10] A.A.C. Alvarez, M. Bibes, W. Prellier, and J. Varignon, Strongly constrained and appropriately normed density functional theory exchange-correlation functional applied to rare earth oxides, Phys. Rev. B 107 (2023) 115109.
[11] A. van de Walle, M. Asta, and G. Ceder, The alloy theoretic automated toolkit: A user guide, CALPHAD Journal 26 (2002) 539.
[12] A. van de Walle, and M. Asta Self-driven lattice-model Monte Carlo simulations of alloy thermodynamic properties and phase diagrams, Modelling Simul. Mater. Sci. Eng. 10 (2002) 521.
[13] P. Söderlind, J. E. Klepeis First-principles elastic properties of α-Pu, Phys. Rev. B 79 (2009) 104110.
[14] L. Chaput, A. Togo, I. Tanaka, and G. Hug, Phonon-phonon interactions in transition metals, Phys. Rev. B 84 (2011) 094302.
[15] C. Kittel, and P. McEuen, Introduction to Solid State Physics, 8th ed., Wiley, New York, 1996.
[16] Z. Tian, K. Esfarjani, G. Chen, Enhancing phonon transmission across a Si/Ge interface by atomic roughness: First-principles study with the Green's function method, Phys. Rev. B 86 (2012) 235304.
[17] F. Zhou, W. Nielson, Y. Xia, V. Ozolins, Lattice anharmonicity and thermal conductivity from compressive sensing of first-principles calculations, Phys. Rev. Lett. 113 (2014) 185501.
[18] A. Van de Walle, G. Ceder, The effect of lattice vibrations on substitutional alloy thermodynamics, Rev. Mod. Phys. 74 (2002) 11.
[19] S. Hao, F. Shi, V. P. Dravid, M. G. Kanatzidis, and C. Wolverton, Computational prediction of high thermoelectric performance in hole doped layered GeSe, Chemistry of Materials 28 (2016) 3218-3226.
[20] S. Hao, V. P. Dravid, M. G. Kanatzidis, C. Wolverton, Computational strategies for design and discovery of nanostructured thermoelectrics, npj Computational Materials 5 (2019) 1-10.
[21] J.E. Saal, S. Kirklin, M. Aykol, B. Meredig, and C. Wolverton Materials Design and Discovery with High-Throughput Density Functional Theory: The Open Quantum Materials Database (OQMD), JOM 65 (2013) 1501-1509.
[22] G. Cao, Y.-H. Wang, Z.-Y. Ding, Z.-G. Liu, J.-H. Ouyang, Y.-M. Wang, Y.-J. Wang, CMAS hot corrosion behavior of rare-earth silicates for environmental barrier coatings applications: a comprehensive review, Heat Treatment and Surface Engineering 3(1) (2021) 9-28.
[23] S. Hao, Z. Lu., C. Wolverton, Quaternary phase diagrams of spinel and composite cathode voltages for concentration gradient materials, Phys. Rev. B 94 (2016) 014114.
[24] S. Hao, J. He, V. P. Dravid, M. G. Kanatzidis, and C. Wolverton, Dimensionally driven crossover from semimetal to direct semiconductor in layered SbAs, Phys. Rev. Materials 3 (2019) 106002.
[25] S. Hao, L.-D. Zhao, C.-Q. Chen, V. P. Dravid, M. G. Kanatzidis, C. Wolverton, Theoretical Prediction and Experimental Confirmation of Unusual Ternary Ordered Semiconductor Compounds in Sr-Pb-S System, J. Am. Chem. Soc. 136 (2014) 1628–1635.

[26] G.J. Redhammer, G. Roth, Beta-($Y_2Si_2O_7$), a new thortveitite-type compound, determined at 100 K and 280 K, Acta Crystallographica C 59 (2003) i103-i106.
[27] Y.I. Smolin, Yu. F. Shepelev, The crystal structures of the rare earth pyrosilicates, Acta Crystallographica B 26 (1970) 484-492.
[28] A.J. Fernandez-Carrion, M. Allix, A. I. Becerro, Thermal expansion of rare-earth pyrosilicates, J. Am. Ceram. Soc. 96 (2013) 2298–2305.
[29] R. Hill, The Elastic Behaviour of a Crystalline Aggregate, Proceedings of the Physical Society. Section A 65 (1952) 349-354.
[30] S.F. Pugh, XCII. Relations between the elastic moduli and the plastic properties of polycrystalline pure metals, Philos. Mag. J. Sci. 45 (1954) 823–843.
[31] Y.-J. Hu, A. Sundar, S. Ogata, L. Qi, Screening of generalized stacking fault energies, surface energies and intrinsic ductile potency of refractory multicomponent alloys, Acta Materialia 210 (2021) 116800.
[32] I.S. Winter, M. de Jong, J. Montoya, E. Rothchild, D.C. Chrzan, Intrinsic ductility of random substitutional alloys from nonlinear elasticity theory, Physical Review Materials 3(11) (2019) 113608.
[33] S. Ogata, J. Li, Toughness scale from first principles, Journal of Applied Physics 106(11) (2009).
[34] N. Wei, X. L. Zhang, C. G. Zhang, S. J. Hou, Z. Zeng, First-principles investigations on the elastic and thermodynamic properties of cubic ZrO_2 under high pressure, International Journal of Modern Physics C 26 (2015) 1550056.
[35] X.-Q. Chen, H. Niu, D. Li, Y. Li, Modeling hardness of polycrystalline materials and bulk metallic glasses, Intermetallics 19 (2011) 1275-1281.
[36] M.D. Dolan, B. Harlan, J. S. White, M. Hall, S. Y. Misture, S. C. Bancheri, B. Bewlay, Structures and Anisotropic Thermal Expansion of the a, b, c and d Polymorphs of $Y_2Si_2O_7$, Powder Diffr. 23 (2008) 20-25.

Appendix

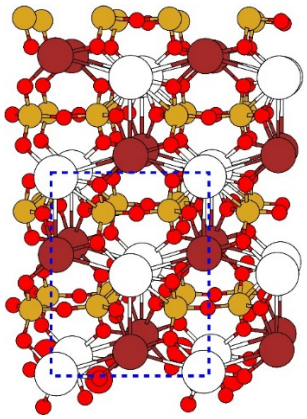

Figure A1 *Atomic structure of ordered stable* $YYbSi_2O_7$ *predicted by the cluster expansion calculations. The white, yellow, dark red big, and small red spheres are Y, Si, Yb, and O, respectively. The space group of the structure is C2 in monoclinic system. The lattice constant a=6.74* Å*, b=8.94* Å*, c=4.71* Å*,* $\alpha = \gamma = 90°$*, and* $\beta = 101.59°$*. The Y and Yb atoms share the original 4g site, Si atoms occupy 4i site, and oxygen reside in 2c,4i, and 8j sites.*